Materials & Design 246 (2024) 113313

Contents lists available at ScienceDirect

Materials & Design

journal homepage: www.elsevier.com/locate/matdes

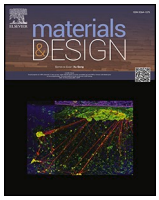

Ultrasonic-induced amorphization and strengthening mechanisms of ultrasonic vibrations assisted friction stir Al/Ti welds

Mingrun Yu [a,b,c], Xinchen Nan [a,b], Li Zhou [a,b,*], Fei Xu [b], Hongyun Zhao [b,*], Xiaoguo Song [a,b]

[a] State Key Laboratory of Precision Welding & Joining of Materials and Structures, Harbin Institute of Technology, Harbin, China
[b] Shandong Provincial Key Laboratory of Special Welding Technology, Harbin Institute of Technology at Weihai, Weihai, China
[c] Research Institute for Advanced Manufacturing, Department of Industrial and Systems Engineering, The Hong Kong Polytechnic University, Hong Kong Special Administrative Region

ARTICLE INFO

Keywords:
Ultrasonic vibrations
Amorphous phase
Al
Ti
Interface evolution
Mechanical properties

ABSTRACT

Integration of aluminum (Al) and titanium (Ti) alloys offers an effective approach to sustainable and high-quality development of the automotive and aviation industries. However, challenges arise when welding Al alloys to Ti alloys due to the formation of detrimental intermetallic compounds at the interface. With the implementation of ultrasonic vibrations, the temperature and strain rate were both increased during Al/Ti friction stir welding (FSW), leading to the formation of an amorphous interlayer, instead of intermetallic compound (IMC), at the interface. The interfacial microcracks were eliminated in the ultrasonic vibrations assisted friction stir welding (UVFSW). There were Ti particles separated from the Ti substrate and dispersed in the Al alloy, thereby resulting in a more gradual and moderate evolution of the interfacial microstructure. Due to the improved interfacial microstructure with ultrasonic vibrations, the lap shear strength was almost twice that of the conventional FSW welds within same welding conditions. Meanwhile, ultrasonic vibrations also improved the fabrication efficiency with a higher optimal traversing speed. The failure mode shifted from interface separation of FSW welds to a shear dimple fracture of the UVFSW welds, demonstrating the better plasticity and reliability of the UVFSW Al/Ti dissimilar joints.

1. Introduction

Joining different materials allows components to achieve favorable mechanical properties while maintaining cost-effectiveness and lightweight design. As a result, dissimilar joining techniques has gained increasing significance in automotive and aviation industries for enhancing product viability and promoting environmental sustainability [1]. The proliferation of electric vehicles and drones emphasizes the urgent necessity for the components with better specific mechanical properties and corrosion resistance [2]. Al/Ti hybrid structures offer ultimate specific strength and corrosion resistance at a reasonable cost, making them widely applicable [3–5]. However, challenges arise when welding Al alloys to Ti alloys, due to their vastly different physical properties and the formation of intermetallic compounds, which cause undesirable residual stress and cracks, weakening the joint [6,7]. Studies on Al/Ti fusion welding, including arc welding [8], laser welding [9], and electron beam welding [10], have highlighted the challenge of suppressing the formation of Al-Ti IMC during the fusion process. In Al/Ti welding, the excessive formation of IMC is caused by the significant variation of mutual solubilities during liquid–solid transition and cooling process, which consequently contributes to the relatively low strength and the propagation of cracks along the interface [11]. Therefore, a high-quality Al/Ti joining method is necessary to control the thickness of interfacial IMC layer at an optimal, thereby improving the strength and reliability of Al/Ti hybrid structures/components.

Friction stir welding (FSW) is a solid-state joining technique that materials are joined through severe plastic deformation with less heat, compared to fusion welding processes [12]. Due to the small diffusivity and solubility in solid state, and as the less heat/energy for IMC nucleation, the formation of interfacial IMC is limited in dissimilar FSW [13–15]. Therefore, Al/steel dissimilar FSW has been deployed in automotive industry, leading to a 25 % reduction of the car body weight

* Corresponding authors at: State Key Laboratory of Precision Welding & Joining of Materials and Structures, Harbin Institute of Technology, Harbin, China (L. Zhou).
E-mail addresses: zhou.li@hit.edu.cn (L. Zhou), hy_zhao66@163.com (H. Zhao).

https://doi.org/10.1016/j.matdes.2024.113313
Received 7 June 2024; Received in revised form 9 August 2024; Accepted 11 September 2024
Available online 12 September 2024

[16]. Researchers shifted to investigate Al/Ti FSW for superior specific strength and lower density. The excessive interfacial IMC, such as $TiAl_3$ and TiAl, was also reported as the primary cause for the fracture of Al/Ti FSW welds [17–19], although their overall strength surpassed that of the conventional welds. The optimal thickness for the interfacial IMC layer was identified to be within 50 nm to 100 nm [20,21]. However, researchers could hardly fabricate the Al/Ti FSW weld with an evenly distributed interfacial layers within this narrow thickness range [22]. Notably, in the FSW Al-Ti welds, TiAl was formed after $TiAl_3$ as a secondary reaction, and required more energy than the formation of $TiAl_3$ [21], suggesting that suppression of the secondary reactions could be a potential approach to controlling the thickness of the IMC layer. Moreover, the tool abrasion not only undermined the cost-effectiveness of Al/Ti FSW, but also damaged the even thickness of IMC layer [23], resulting in the heterogeneous interfacial microstructure and mechanical properties [24]. In an effort to avoid tool abrasion, researchers introduced interlayers between Al and Ti substrates during the FSW process [25–27]. However, interlayer-assisted FSW necessitated additional preparatory work prior to welding, thereby increasing the costs and time in practical fabrication [28]. Considering these challenges, there is an urgent need for a welding process that can fabricate reliable Al-Ti welds and avoid tool wear simultaneously.

Ultrasonic vibrations assisted friction stir welding (UVFSW) is an innovative approach for the fabrication of dissimilar joints with desirable strength, but no additional preparation [14,29–31]. This technique, which emerged in the late 2010s, conducted ultrasonic vibrations on the welding plates to improve material deformation and weld formation during the FSW process [32]. The introduction of ultrasonic vibrations during the FSW process exhibited several beneficial effects as follows. Firstly, the acoustic softening effect of ultrasonic vibrations was demonstrated in UVFSW [33], resulting in the elimination of inner defect [34], expanded welding area [35], and reduction on spindle torque [36]. Secondly, the ultrasonic vibrations lowered the peak welding temperature [37], resulting in the smaller grain sizes of weld zones [38]. Specific to welding of dissimilar materials, UVFSW exhibited better welding strength due to the suppression on the formation IMC [39]. Not only was the overall volume of IMCs diminished, but the species of IMC were also reduced during dissimilar UVFSW [40–42], leading to the improved weld integrity. Additionally, UVFSW was reported to mitigate tool abrasion [43], which was a common challenge in Al/Ti FSW.

Notwithstanding aforementioned promising advancements, the existing studies on Al/Ti UVFSW remains far from systematical. Present studies have primarily focused on numerical simulation of material flow, identification of interfacial phases, and evaluation of mechanical properties, while the underlying improvements on the bonding mechanism facilitated by ultrasonic vibrations remain unclear. Further investigations are necessary to fully elucidate the relationship between the interfacial microstructure and the resulting weld strength. Moreover, comprehensive studies on the influence of key welding parameters, such as traversing speed, on the corresponding microstructural evolution and mechanical performance are required. In the present study, the ultrasonic vibrations were used to improve the metallurgically bonding of the Al/Ti lap welds without stirring Ti substrate. The welding temperature profiles have been recorded, providing critical insights into the ultrasonic-induced amorphization by which ultrasonic vibrations improve the bonding process. Furthermore, the welding parameters have been optimized based on the resultant lap shear strength, and the relationship between interface evolution, mechanical properties, and fracture behavior of the joints has been proposed. The experimental findings from this study offer a scientific foundation for understanding the beneficial impacts of incorporating ultrasonic vibrations into the friction stir welding of dissimilar metals. The ultrasonic-induced amorphization and the proposed correlations between microstructure and mechanical properties serve as a valuable knowledge base to drive further investigation and industrial adoption of this innovative joining technique.

Table 1
Chemical compositions of the base materials.

Base materials	Elements (At. %)				
	Al	Mg	Si	Ti	V
AA6061	Bal.	1.43	0.62	–	–
Ti6Al4V	9.93	–	–	Bal.	3.91

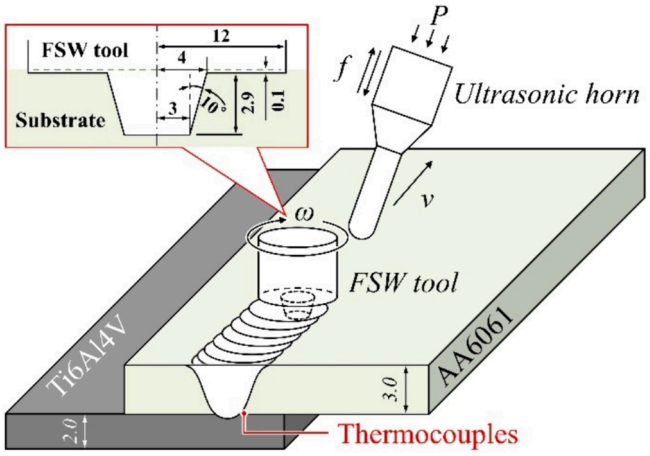

Fig. 1. Configuration of the AA6061/Ti6Al4V UVFSW.

Table 2
Welding conditions in this work.*

No.	FSW parameters		Ultrasonic parameters		
	Traversing speed (v, mm/min)	Rotational speed (ω, rpm)	Amplitude (μm)	Pressure (P, MPa)	Tilt angle (θ, deg.)
1	60	1000	10	0.5	30
2	80				
3	100				
4	120				
5	140				

* In each of the selected welding conditions, the welding process was repeated without ultrasonic vibration as a control.

2. Materials and experimental procedure

UVFSW have been conducted on the AA6061 and Ti6Al4V plates with the dimensions of 75 mm × 250 mm × 3 mm and 75 mm × 250 mm × 2 mm, respectively. The chemical compositions of the base materials (BM) are listed in Table 1. During welding, the Al plate was placed on the Ti plate at the retreating side (RS), as depicted in Fig. 1. This configuration was reported achieving superior performance compared to the alternative of placing the Ti plate on top [44,45]. The traversing speed (v) was varied from 60 mm/min to 140 mm/min with an interval of 20 mm/min, whereas the rotational speed was constant at 1000 rpm. The stirring tool was composed of a 12.0 mm wide shoulder and a 2.9 mm long pin. The stirring tool was thus supposed not to touch the Ti substrate, as the thickness of Al plate equaled to the sum of pin length and shoulder plunging depth. Furthermore, type-K thermocouples were positioned at the bottom of Al plates to record the temperature history at the advancing side (AS) with a distance of 2.0 mm from the weld center. In UVFSW, the ultrasonic vibrations were remained at 20 kHz with an amplitude of 10 μm and pressure of 0.3 MPa, which was reported as the preferable choice in Al/Ti welding [43]. The ultrasonic horn was placed 30 mm ahead of the stirring tool with a tilting angle of 30°, and the

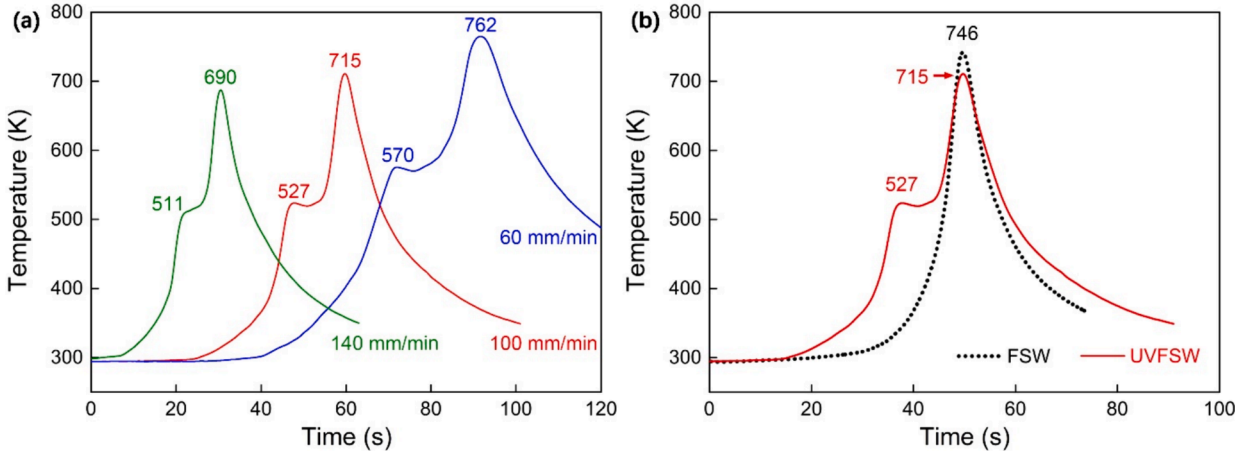

Fig. 2. Temperature histories of Al/Ti welding: (a) UVFSW temperature at various traversing speeds, (b) FSW and UVFSW temperature (v = 100 mm/min).

detailed welding parameters were listed in Table 2. In each of the selected welding conditions, welding process was repeated without ultrasonic vibrations as a control.

Following the welding processes, specimens were cut perpendicular to the welding direction by an electrical discharge machine (DM-Cut 6531), for subsequent metallographic analysis and mechanical tests. The microstructure characteristics were observed via optical microscopy (OM, DSX 510), scanning electron microscopy (SEM, MERLIN Compact), and transmission electron microscopy (TEM, JEM-2100). The metallographic specimens intended for optical observation were etched using Keller's etchant (1.0 ml HF+1.5 ml HCl + 2.5 ml HNO3 + 95 ml H2O). Meanwhile, the energy-dispersive X-ray spectrometry (EDS, OCTANE PLUS), X-ray diffractometer (XRD, D/max-2500), and selected area electron diffraction (SAED) were employed to analyze chemical compositions and phase identification. The metallographic specimens intended for optical observation were etched using Keller's etchant (1.0 ml HF+1.5 ml HCl + 2.5 ml HNO_3 + 95 ml H_2O). Lap shear tests were conducted via a universal testing machine (Instron 5967), referring to the standard ASTM D1002-10. The lap shear tests were repeated three times for each weld at a crosshead speed of 1 mm/min, using the 10.0 mm wide specimens.

3. Results and discussion

3.1. Welding temperature and cross-section

Temperature variations in UVFSW and FSW are shown in Fig. 2, as a function of time. The temperature history of Al/Ti UVFSW includes ultrasonic heating period and friction heating period, which were attributed to the different heating sources. The interfacial temperature was firstly increased over 500 K due to the heating effect of ultrasonic vibrations, and then further increased to a peak temperature around 700 K due to the friction heat generated by stirring process. As the traversing speed changed, the increase of traversing speed led to the reduction of peak temperatures. At 60 mm/min, the peak temperature was 570 K at ultrasonic heating period, whereas 762 K at the friction heating period. When the traversing speed was increased, the peak temperatures were decreased to 527 K and 715 K at 100 mm/min, and to 511 K and 690 K at 140 mm/min, respectively. This was because an increase of traversing speed resulted in a decrease of heat input, which was the welding energy supplied per millimeter and inversely proportional to the traversing speed (ω^2/v) [12]. Compared to the conventional FSW, UVFSW has an additional heating process before reaching the highest temperature, namely the ultrasonic heating mentioned above. But the maximum temperature was decreased by ~5 % in UVFSW, because the acoustoplastic effect of ultrasonic vibrations improved the flowability of weld metals, reduced friction heat, and finally led to the decrease of maximum temperature [33].

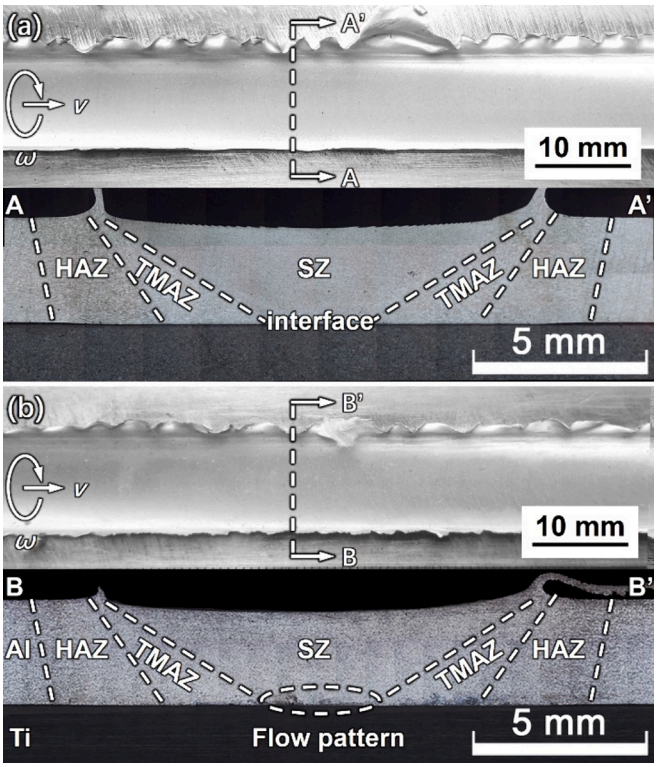

Fig. 3. Appearance and cross-sections of Al/Ti welds (v = 100 mm/min): (a) FSW weld, (b) UVFSW weld.

Fig. 3 shows the appearances and cross-sections of the FSW and UVFSW Al/Ti welds at 100 mm/min. Flashes only formed on the retreating side of the FSW weld. But there were continuous flashes formed on both sides of the UVFSW, because the flowability of weld metal was promoted by ultrasonic vibrations. As for the cross sections, the Al/Ti welds were composed of heat affected zone (HAZ), thermos-mechanically affected zone (TMAZ), stir zone (SZ), and interface. Compared to the conventional FSW weld, there were additional flow patterns formed at the interface of the UVFSW weld, which indicates that ultrasonic vibrations improved the flowability of titanium alloy and enhanced intermixing of matrixes during welding.

Fig. 4 listed the metallographic images and grain sizes of the weld zones within various welding conditions. The grain sizes were measured

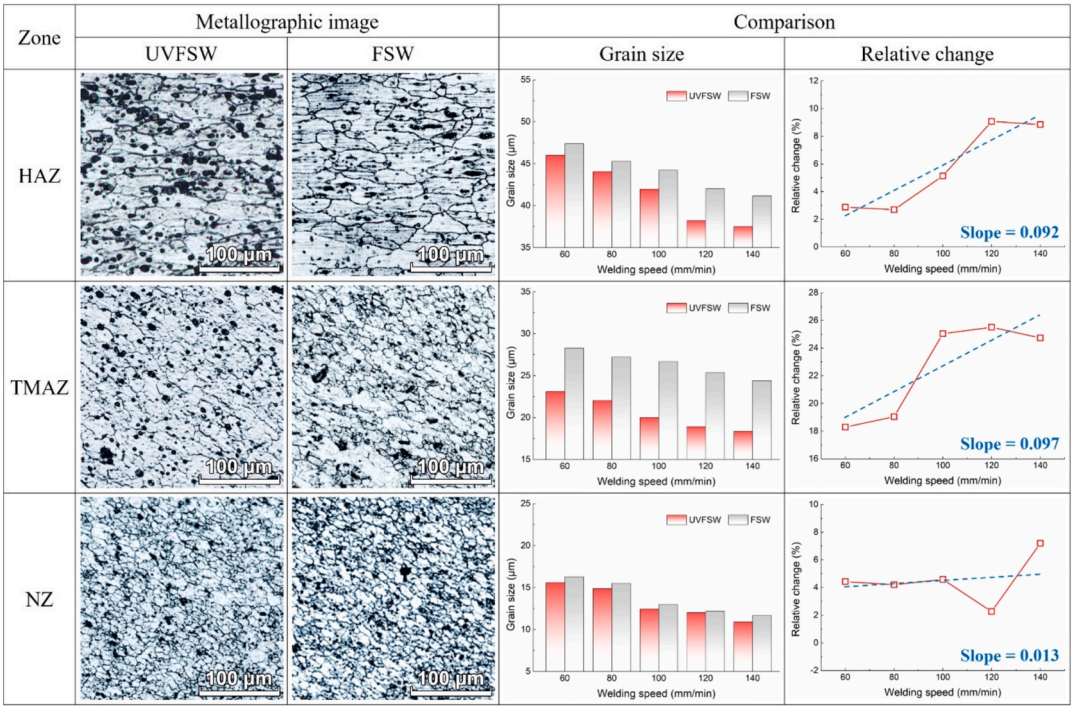

Fig. 4. Metallographic images and grain sizes in various welding conditions.

by Average Grain Intercept method referring to ASTM E112. The HAZ grains were subjected to a thermal cycle but is not deformed during either FSW or UVFSW. Therefore, the microstructure was recognizably that of the base metal, but coarsened. The grain size of the HAZ of UVFSW weld was smaller than that of the FSW weld, due to the lower temperature with ultrasonic vibrations mentioned above. The TMAZ was formed as a transition zone between the SZ and HAZ. In this region, material experienced both thermal cycle and deformation during welding, and the grains were significantly deformed and rotated, judging from the morphology of the base metal. The metals in SZ experienced heavily deformation and recrystallization during FSW or UVFSW. As a result, the SZ was composed of equiaxed grains with a smaller size than that in the base metals. According to the variation of grain size, the influence of ultrasonic vibrations was most significant in TMAZ, whereas least in SZ. The ultrasonic enhancement on the flowability of weld metal in UVFSW led to higher strain rate in TMAZ and recrystallization on some grains, resulting the smaller grain size. However, the influence of ultrasonic vibrations was almost eliminated in SZ, because the grains were fully recrystallized after welding, and, thereby, the grain size was mainly affected by temperature. In addition, difference between the grain sizes of UVFSW and FSW was reduced with the decreasing traversing speed, suggesting that influence of ultrasonic vibrations on the microstructure was more significant at higher traversing speed.

The grain size (d) of the welded aluminum alloy was closely related to the deformation and heat depending on the Zener-Hollomon parameter (Z):

$$d^{-1} = AlnZ + B = A\varepsilon exp\left(\frac{Q}{RT}\right) + B \tag{1}$$

where A and B are empirical constants, ε is the strain rate of deformation, Q is the activation energy for deformation, R is gas constant, and T is temperature. The empirical constants A and B were referred to previous study [46], and the activation energy for the deformation of base material was 236 kJ/mol [47]. Therefore, the strain rate could be expressed by the following equation.

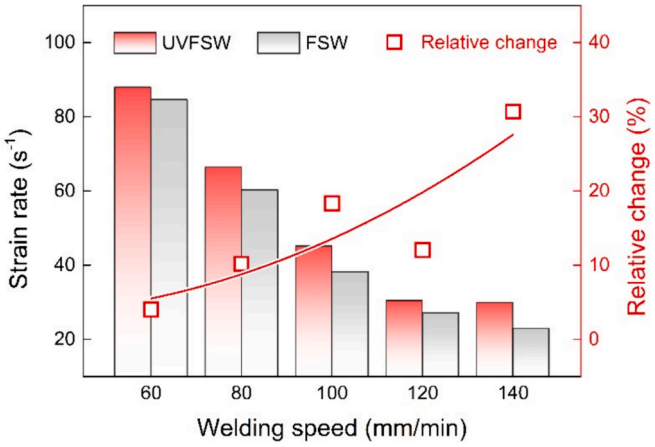

Fig. 5. SZ strain rates in various welding conditions.

$$\varepsilon = \left(d^{-1} - B\right)A^{-1}\exp\left(\frac{RT}{Q}\right) \tag{2}$$

The strain rates were calculated and shown in Fig. 5, basing on the aforementioned grain and the average temperature of stirring period, which was duration after the peak temperature with a lasting time equaled to the tool diameter divided by welding speeds. The strain rate of UVFSW was increased by 3.39 s^{-1}at 60 mm/min, which was equivalent to 4.01 % of that in FSW. When the traversing speed was increased to 140 mm/min, the variation of strain rate between UVFSW and FSW was increased to 7.03 s^{-1}, and the relative change was increased to 30.67 %. These results indicated that ultrasonic vibrations enhanced the flowability of weld metal during FSW. Furthermore, it was observed that as the traversing speed was increased, the promoting effect induced by the ultrasonic vibrations became more pronounced.

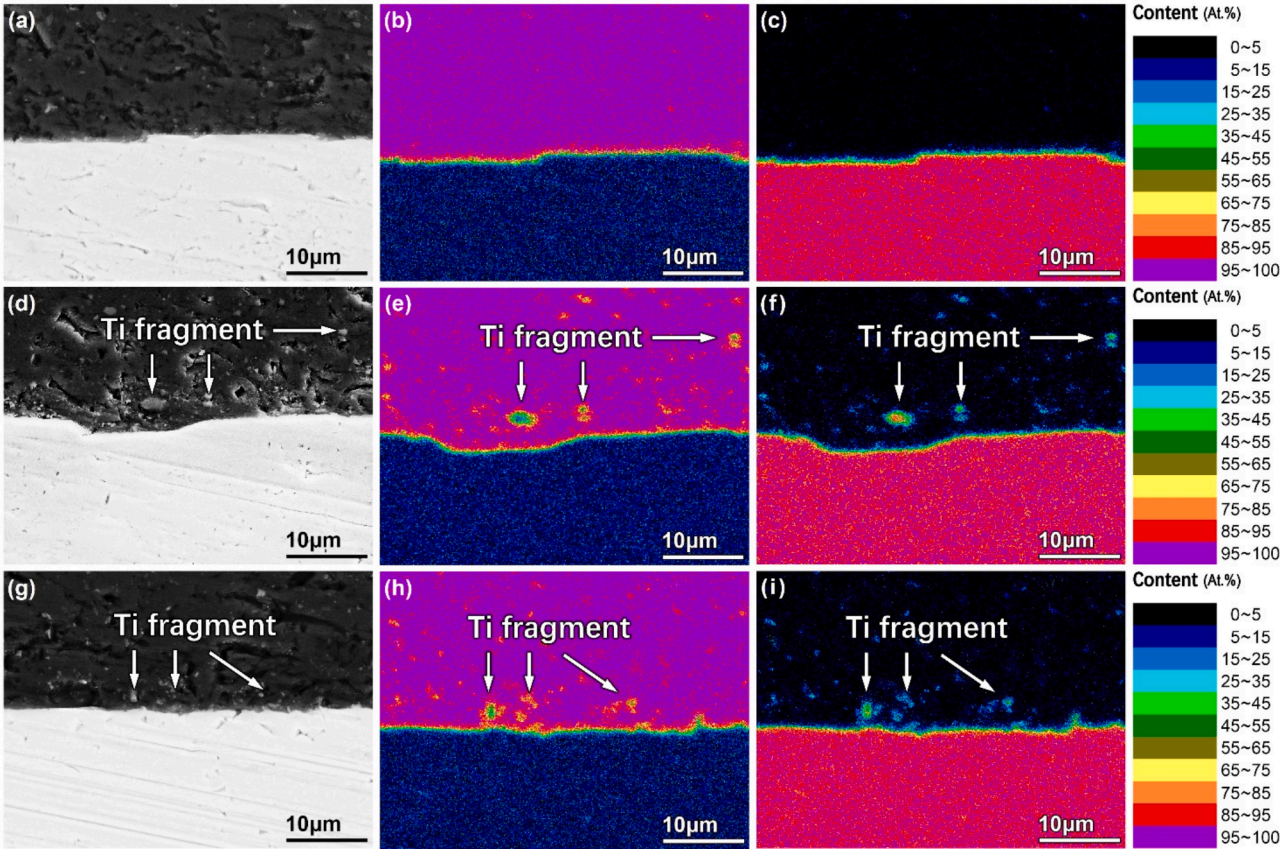

Fig. 6. UVFSW interfaces at various traversing speeds: (a) SEM image, (b) Al map, and (c) Ti map at 60 mm/min; (d) SEM image, (e) Al map, and (f) Ti map at 100 mm/min; (g) SEM image, (h) Al map, and (i) Ti map at 60 mm/min.

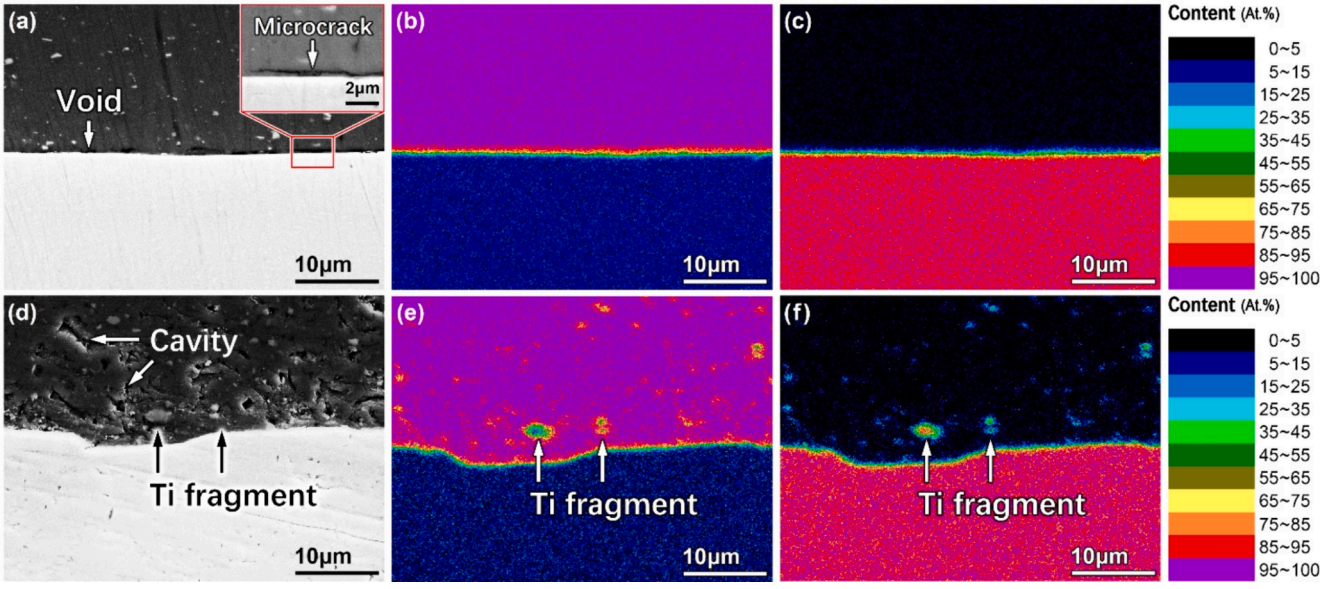

Fig. 7. Comparison between the FSW and UVFSW interfaces: (a) SEM image, (b) Al map, and (c) Ti map of FSW interface; (d) SEM image, (e) Al map, and (f) Ti map of FSW interface.

3.2. *Interfacial microstructure*

Interface evolution and element distribution with increasing traversing speed in UVFSW are shown in Fig. 6, including the SEM images, and EDS maps of aluminum and titanium. According to the element distributions at 140 mm/min, the Ti alloy was broken partly at the UVFSW interface, and Ti fragments were observed in the Al alloy. The Ti fragments could cause the initiation of cracks in mechanical tests, while enhancing the grain refinement during dynamic recrystallization. The presence of Ti fragments in Al alloy was also observed at 100 mm/min, while exhibiting a trend of being farther away from the interface. As the traversing speed further decreased to 60 mm/min, the Ti

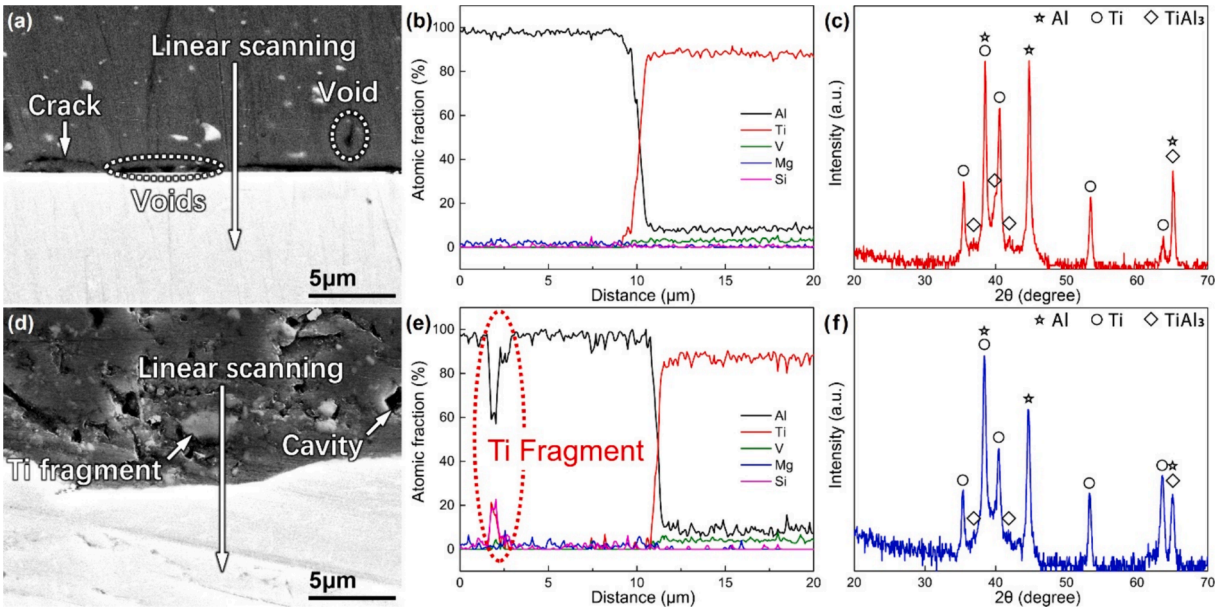

Fig. 8. SEM and XRD results of FSW and UVFSW interfaces ($v = 100$ mm/min) with high magnification: (a) SEM image, (b) linear EDS, and (c) XRD spectrums of FSW interface; (d) SEM image, (e) linear EDS, and (f) XRD spectrums of UVFSW interface.

fragments almost disappeared from the interface, which could be attributed to the farther dispersion caused by the promoted material flow at low traversing speed. This indicated that, in UVFSW, the ultrasonic vibrations broke the surface of Ti substrate at first, and, then, the stirring and friction process from the FSW tool moved the fragments away from the substrate, resulting in the formation of Ti fragments in Al alloy.

Fig. 7 exhibits the interfacial microstructure and element

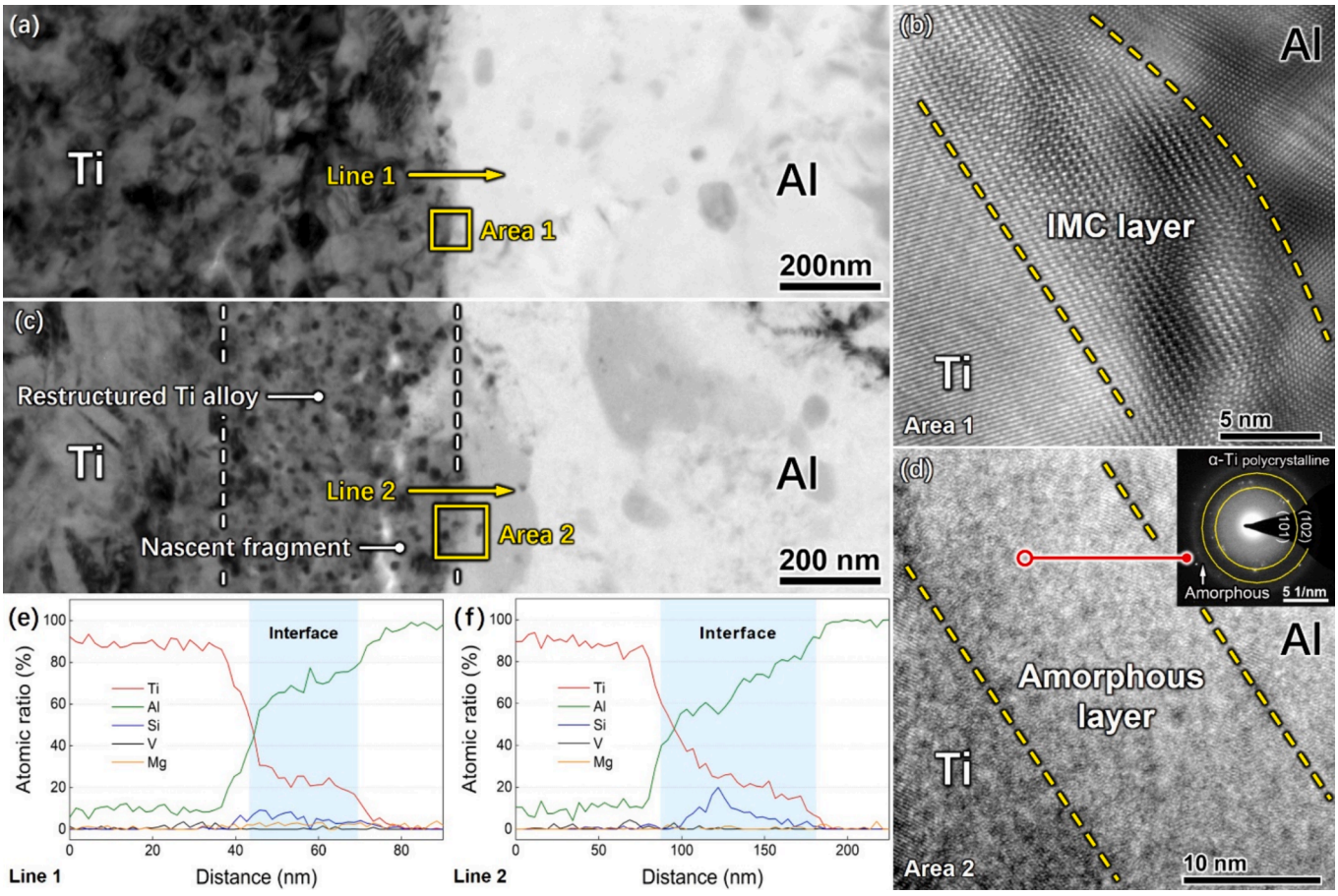

Fig. 9. TEM results of the FSW and UVFSW interfaces ($v = 100$ mm/min): (a) bright field image and (b) high resolution image of FSW interface, (c) bright field image and (d) high resolution image of UVFSW interface, (e) elemental composition of line 1, (f) elemental composition of line 2.

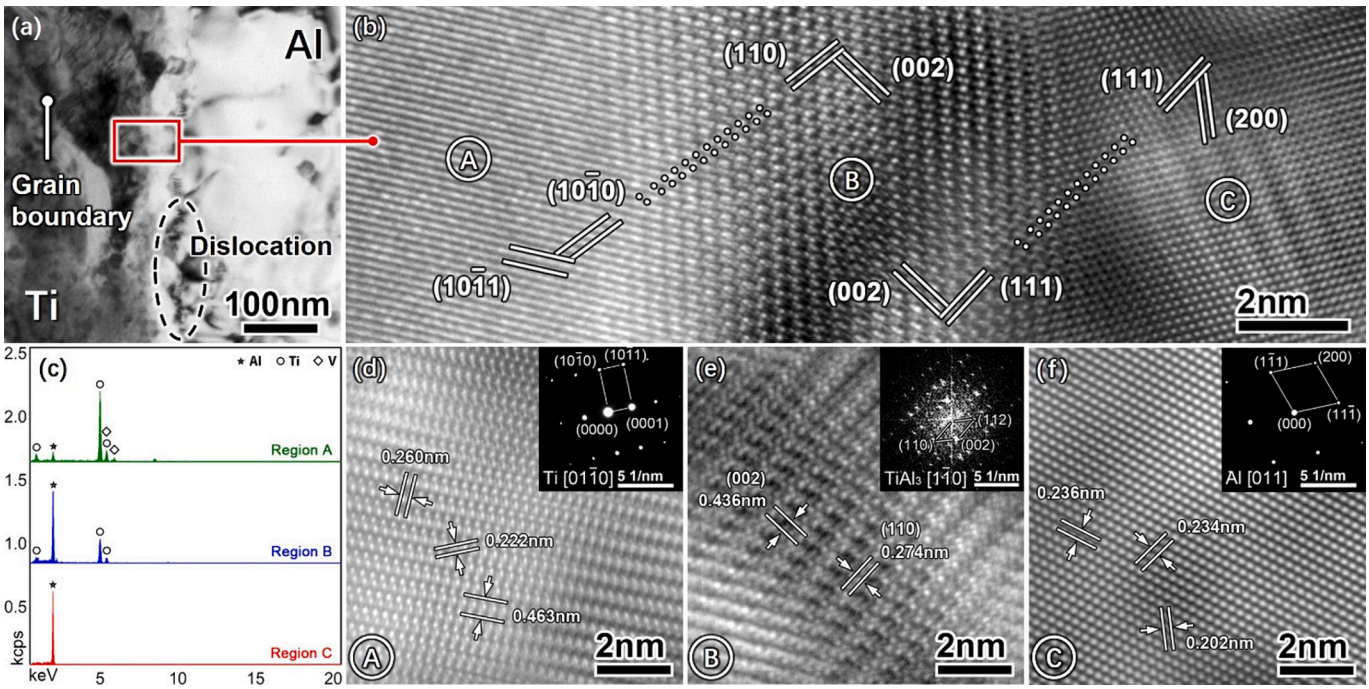

Fig. 10. High magnification TEM results of TEM interface: (a) bright field image; (b) overview and (c) EDS spectrums of areas A-C; high magnification images and electron diffraction patterns of (d) area A, (e) area B, and (f) area C.

distribution of the FSW and UVFSW Al/Ti welds at 100 mm/min. There was no visible mixture of Al and Ti alloys, but welding defects formed at the FSW interface, including micro-cracks and voids, which would weaken the welds remarkably [48]. In the UVFSW weld, ultrasonic vibrations eliminated the voids and micro-cracks at the interface. The elimination of interfacial defects indicated the improvements not only on the flowability of Al alloy, but also on the atomic migration and intermixing, which could result in a better bonded interface. Moreover, ultrasonic vibrations induced Ti fragments and cavities in the Al alloy. The formation of Ti fragments was resulted from the collapse of the ultrasonic cavities, which could emit shock waves and thereby break the surface of Ti substrate [43], and the Ti fragments were intermixed into the Al alloy due to the stirring process from the FSW tool following the ultrasonic horn. Once the strain rate and temperature rapidly dropped before the cavity collapse, the unclosed cavities were remained in the Al alloy, leading to the formation of unexpected cavities or pores in the SZ, as marked in the SEM image.

Fig. 8 shows the magnified images, EDS linear results, and XRD spectrums of the FSW and UVFSW interfaces welded at 100 mm/min. According to the high-magnification SEM image, the cracks and voids were formed not only along the FSW interface, but also in the aluminum alloy. According to the SEM image and EDS linear results, there was no visible intermetallic compound at the FSW interface, whereas diffraction peaks of the intermetallic compound, $TiAl_3$, were shown on the XRD spectrums. As for the UVFSW interface, the interfacial crack and void were eliminated, but more cavities were formed in the Al alloy. According to the EDS linear result, no visible intermetallic compound was formed at the interface, but the composition around Ti fragment was close to that of $TiAl_3$. The diffraction peaks of $TiAl_3$ were also found on the XRD spectrums of UVFSW interface, whereas the intensity was lower than that of the FSW interface.

3.3. Formation of interfacial phases

Fig. 9 shows the bright field and higher resolution TEM images, and EDS liner results of the FSW and UVFSW interfaces welded at 100 mm/min. At the FSW interface, the Al and Ti alloys were metallurgically bonded via the formation of IMC layer with an approximate thickness of 10 nm. Upon the application of ultrasonic vibrations during welding, the Al and Ti alloys were metallurgically bonded through an amorphous layer formed at the interface, replacing the IMC layer, due to the reduced peak temperature. In addition, the Ti alloy adjacent to the interface was restructured, forming the nanocrystalline titanium, and partly fragmented, since ultrasonic vibrations were applied during FSW. According to the EDS linear results, the amorphous layer was mainly composed of aluminum, titanium, silicon (Si), and magnesium (Mg), and the Si composition was relatively higher, as compared to the IMC layer. The diffusion distances of the titanium atoms within the aluminum alloy was significantly greater than that observed at the FSW interface, which was attributed to the enhanced atomic migration facilitated by ultrasonic vibrations and severer deformation during the UVFSW. These results indicated that the ultrasonic vibrations had a promoting impact on the atom migration and intermixing, leading to the formation of amorphous layer. Concurrently, the ultrasonic effects were confined primarily to the immediate vicinity of the interface, likely due to the excellent elasticity inherent to the metallic glass [40].

Table 3
Elemental compositions of the selected areas in Figs. 10 and 11.

Areas	Elements (At. %)				
	Al	Ti	V	Mg	Si
A	13.5	83.1	3.3	0.1	0.1
B	72.6	23.6	1.3	08	1.8
C	98.3	0.0	0.0	1.3	0.4
D	13.0	80.6	4.7	1.4	0.3
E	70.5	22.3	1.7	0.3	5.3
F	87.8	8.7	0.8	1.1	1.6

Detailed interfacial microstructure of the FSW interface welded at 100 mm/min was shown in Fig. 10, and the chemical composition of the selected areas are listed in Table 3. There were dislocations blocked around the interface with no visible formation of intermetallic products, according to the bright field image. However, as shown in the high-resolution images and energy dispersive spectrums, an intermetallic

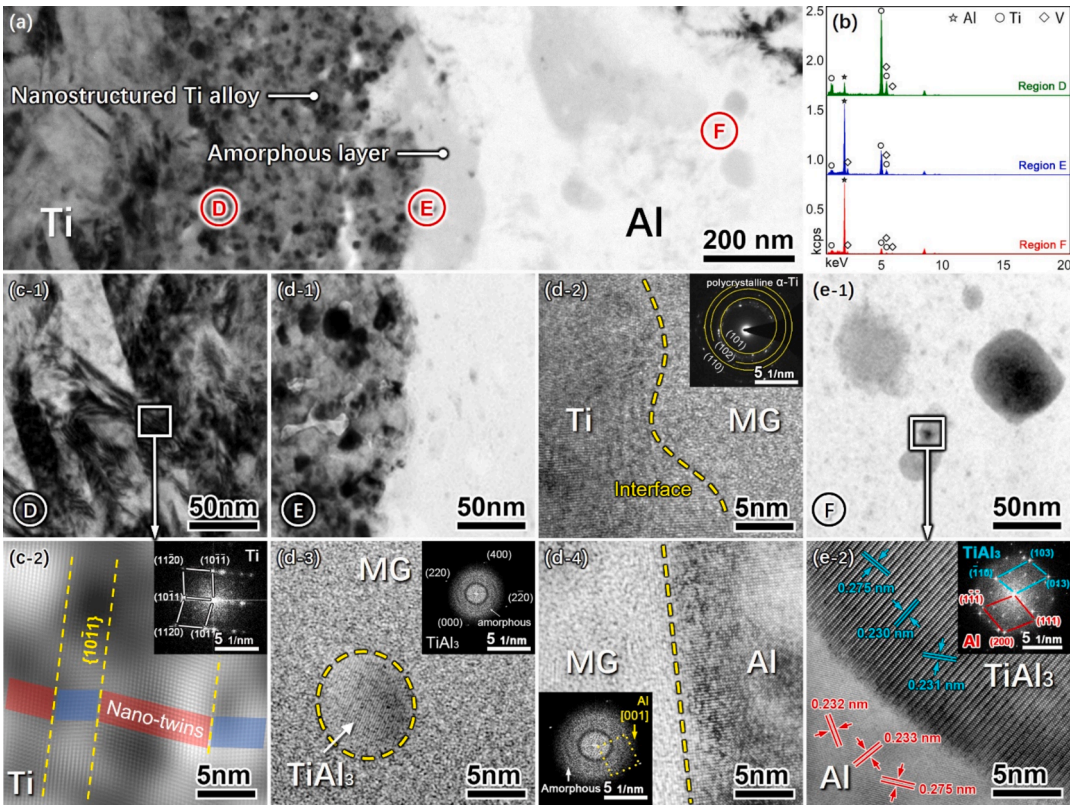

Fig. 11. High magnification TEM results of UVFSW interface: (a) overview image, and (b) EDS spectrums of selected areas D-F; high magnification images and electron diffraction patterns of (c) area D, (d) area E, and (e) area F.

layer of $TiAl_3$ was formed at the interface, bonding the Al and Ti substrates metallurgically. The interfacial orientation relations were revealed from the high-resolution TEM image, suggesting the lattice plane <01_10> of titanium parallel to the planes <1_10> of $TiAl_3$ and <01_1> of aluminum. Accordingly, the lattice mismatches at the interface were 6.95 % between the Ti alloy and $TiAl_3$ layer, and 4.91 % between the $TiAl_3$ layer and the Al alloy, which were much smaller than the theoretical mismatch of 11.85 % between the Ti and Al planes. This indicated that the formation of the $TiAl_3$ layer could reduce the lattice mismatch at the Ti/Al interface, which could relieve the lattice distortion and related stress at the incoherent interface [49]. However, the formation of intermetallic compounds just reduced, rather than eliminating, the lattice distortion at the interface. Therefore, the ultrasonic vibrations were applied to assist the Al/Ti FSW, in order to eliminate or further reduce the lattice distortion, and thereby improve the welding strength.

Further magnified TEM results of the UVFSW interface welded at 100 mm/min was shown in Fig. 11, and the chemical composition of the selected areas are listed in Table 3. Since influenced by the promoted deformation in UVFSW, the Ti alloy was partially restructured, forming the fairly equiaxed nanograins and nanotwins at the interface beside the amorphous layer. Therefore, the substrates were metallurgically bonded through the Ti/nano-Ti/amorphous/Al interface in UVFSW instead of the aforementioned $Ti/TiAl_3/Al$ interface in FSW. In the nanostructured titanium area, the {10_11} twins were found roughly parallel to the interface, which could simultaneously enhance the ductility and strength of the weld during bearing the shear loads parallel to the interface [50]. The formation of amorphous layer could further reduce the interfacial lattice distortion, due to the absence of lattice structure, and improve the stress tolerance of the interface, as the amorphous metals commonly exhibited higher strength and elastic modulus than the polycrystalline metals with similar compositions [51]. Moreover, as

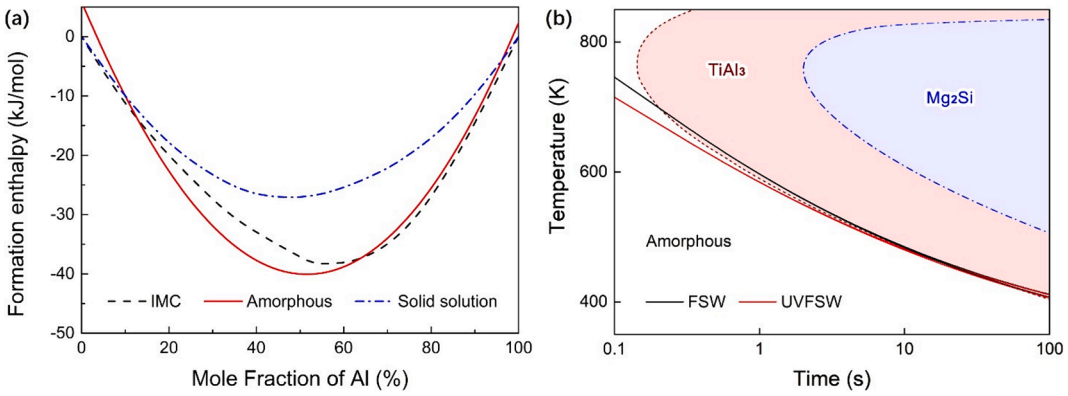

Fig. 12. Thermodynamics in Al-Ti system: (a) formation enthalpy curves, (b) temperature–time-transformation curves.

shown in the high-resolution images, homogeneous nucleation of $TiAl_3$ was observed in the amorphous layer, suggesting that the IMC at the UVFSW interface could be formed through the homogeneous nucleation in the amorphous layer rather than the heterogeneous nucleation between the base metals. As mentioned in the EDS linear results, excessive Ti atoms were diffused into the Al alloy. Therefore, in proximity to the interface, the Ti content exceeded the solubility within the Al alloy, leading to a state known as oversaturation. Tiny $TiAl_3$ precipitates were formed in the oversaturated Al alloy, lowering the Ti content of the Al matrix. The intermetallic precipitates impeded the movement of lattice defects, such as dislocation, in the base alloy, which could enhance the interfacial strength and hardness [52].

Formation of amorphous phase at Al-Ti interface was further investigated using the enthalpy-composition curves and temperature–time-transformation (TTT) curves shown in Fig. 12. According to the Miedema's semi-empirical model, the elastic enthalpy (ΔH^{ela}) and structural enthalpy (ΔH^{stru}) are absent, whereas there is topology enthalpy (ΔH^{topo}), in the formation of amorphous phases [53]. Therefore, the formation enthalpies of amorphous alloys (ΔH^{amor}), solid solution (ΔH^{ss}), and intermetallic compounds (ΔH^{inter}) can be calculated via following equations.

$$\Delta H^{amor} = \Delta H^{chem}(\text{amor}) + \Delta H^{topo} \tag{3}$$

$$\Delta H^{ss} = \Delta H^{chem}(\text{ss}) + \Delta H^{ela} + \Delta H^{stru} \tag{4}$$

$$\Delta H^{inter} = \Delta H^{chem}(\text{inter}) \tag{5}$$

where $\Delta H^{chem}(amor)$, $\Delta H^{chem}(ss)$, and $\Delta H^{chem}(inter)$ are the chemical mixing enthalpies of amorphous phase, solid solution and IMC, respectively. The elastic enthalpy and topology enthalpy can be expressed as [53]:

$$\Delta H^{topo} = 3.5\sum_{i=1}^{n} x_i T_{m,i} \tag{6}$$

$$\Delta H^{ela} = \frac{2\mu_j (V_i - V_j)^2}{V_j\left(3 + 4\mu_j K_i\right)} \tag{7}$$

where x_i represents the mole fraction of component i, and $T_{m,i}$ is the melting temperature of component i. μ_j is the shear modulus of the solvent, V_i and V_j are the molar volumes of the solute and the solvent, respectively, and K_i is the compressibility of the solute. The formation enthalpies in Al-Ti system were calculated at 700 K, as shown in Fig. 12a. According to the calculated formation enthalpies, the formation enthalpy of amorphous phase was lower than that of the solid solution or IMC within the Al fraction range of 15 % to 60 %, which corresponded to the experimental results in previous studies [54]. Moreover, the differences between the interfacial formation in UVFSW and FSW were explored using the time–temperature-transformation (TTT) curves. The time (t) needed to for a volume fraction X of the transformed crystalline phase in an undercooling system can be given by the following expression [55].

$$t \approx \frac{9.3\eta}{kT}\left\{\frac{a_0^9 X}{f^3 N_v} \bullet \frac{exp\left(\frac{\Delta G^*}{kT}\right)}{\left[1 - exp\left(\frac{-\Delta G_m}{RT}\right)\right]^3}\right\}^{\frac{1}{4}} \tag{8}$$

where T is the temperature, η is the viscosity, a_0 is the atomic diameter, f is a structural constant, N_v is the number of atoms per unit volume, ΔG^* is the Gibbs energy barrier to nucleation and ΔG_m is the driving force for nucleation, R is the gas constant. Referring to the previous studies [55–57], the TTT curves with a Ti fraction of 20 %, corresponding to the interface, was shown in Fig. 12b, accompanied with cooling curves of FSW and UVFSW processes. The FSW cooling curve developed into the $TiAl_3$ area at the nose of the TTT curve, indicating the formation $TiAl_3$. Due to the lower peak temperature, the UVFSW cooling curve had a lower start, and developed out of the $TiAl_3$ area until 15 s. Therefore, the intermetallic compounds were formed after a 15-second experience of amorphous formation in UVFSW, which was in accordance with the TEM results above.

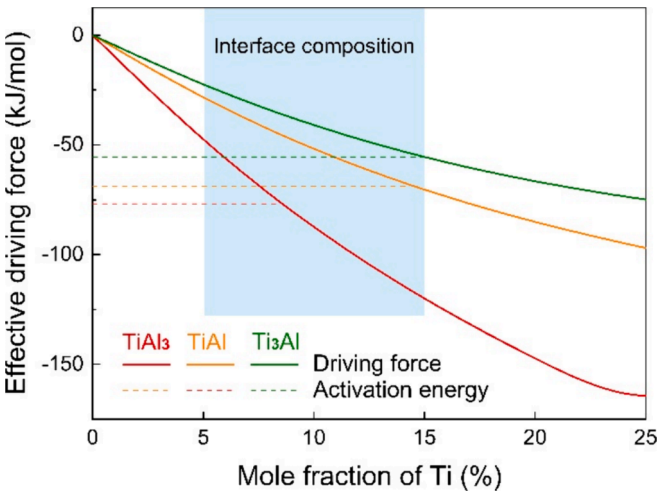

Fig. 13. Driving forces of Al-Ti intermetallic compounds.

Table 4
Free energies and bonding strengths in Al-Ti system (725 K, kJ/mol) [58].

G^0_{Al}	G^0_{Ti}	u_{Al-Ti}	u_{Ti-Ti}	u_{Al-Al}
−92.44	−99.71	263.4	138.8	264.3

Driving forces with Ti fraction, as shown in Fig. 13, were utilized to investigate the nucleation of the IMC at the interface and in the oversaturated Al alloy. The driving force (ΔG_m) represented the free energy required to form the IMC per mole, which could be calculated from partial mole free energies of the Al-Ti system as follows [21]:

$$\Delta G_m = \frac{\partial G_m(x_e)}{\partial x_e}\left(x_e^{IMC} - x_e\right) + \left[G_m(x_e) - G^0_{IMC}\right] \tag{9}$$

where $\frac{\partial G_m(x_e)}{\partial x_e}$ is the partial derivative of the free energy of the solution (G_m) with respect to the mole fraction of the limiting element (x_e) at interface, x_e^{IMC} is the mole fraction of the limiting element in the nucleating IMC, and G^0_{IMC} is the integral free energy of the nucleating IMC. The free energy of the solution (G_m) can be expressed by the following equation [58].

$$G_m = \sum_{1=1}^{n} x_i G_i^0 + RT\sum_{1=1}^{n} x_i \ln x_i + zN_A\left[u_{Al-Ti} - \frac{(u_{Ti-Ti} + u_{Al-Al})}{2}\right] \bullet \prod_{i=1}^{n} x_i \tag{10}$$

where x_i and G_i^0 are the mole fractions and the integral free energies of elements in the solution, respectively. z is the coordination number; N_A is the Avogadro constant. u_{Al-Al}, u_{Al-Ti} and u_{ATi-Ti} are the bonding energies of Al-Al, Al-Ti and Ti-Ti bonds, respectively. The effective driving force (ΔG_m^e) could be derived from the standard driving force and the interfacial composition as follow:

$$\Delta G_m^e = \Delta G_m \bullet \frac{x_e}{x_e^{IMC}} \tag{11}$$

The calculation of the driving forces was conducted using the data listed in Table 4. The driving force of the formation of $TiAl_3$ surpassed the

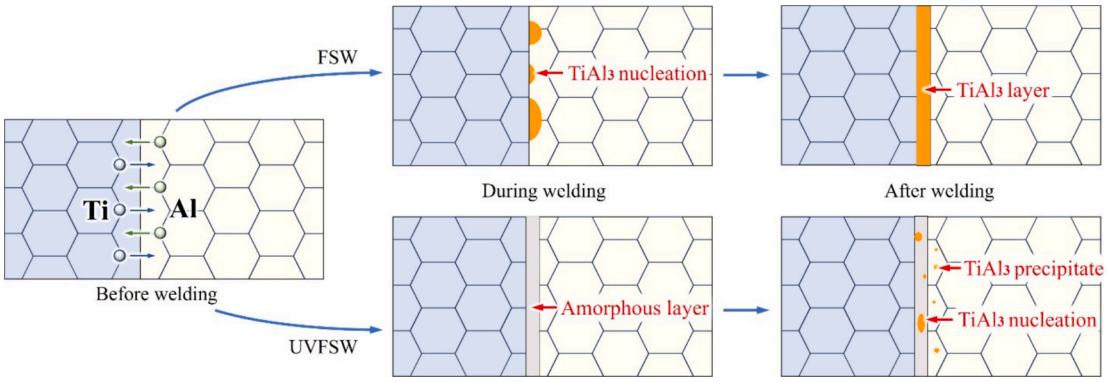

Fig. 14. Schematic diagrams of the interface evolution in FSW and UVFSW.

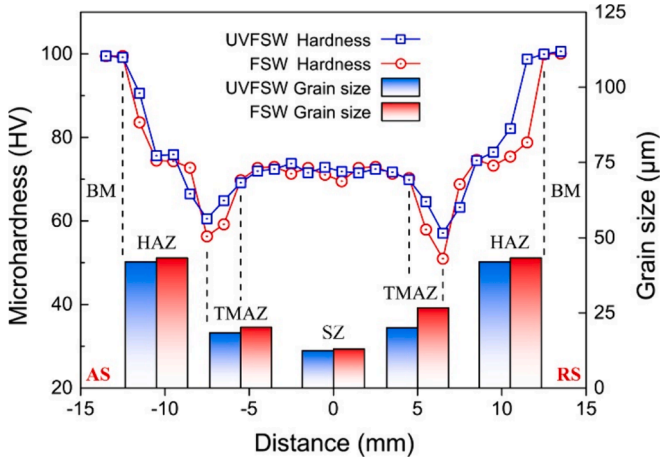

Fig. 15. Microhardness tested along the middle line parallel to the Al/Ti interface of the UVFSW and FSW welds.

energy barrier with a Ti fraction over 8.6 %, whereas for TiAl and Ti_3Al, the corresponding thresholds are 14.5 % and 15.2 %, respectively. In view of that the interfacial reactions during FSW are transient and non-equilibrium, there was no sufficient energy the second-set reactions, which used $TiAl_3$ as reactant [21]. Therefore, $TiAl_3$ should be the primary product at the UVFSW and FSW interfaces. The energy barriers were calculated from the experimental results in previous studies [59], using the Arrhenius equation.

$$k = A \bullet exp\left(\frac{-E_a}{RT}\right) \tag{12}$$

where k is the growth rate, A is the pre-exponential factor, and E_a is the activation energy, which is also known as energy barrier or activation barrier.

The schematic illustration shows the formation processes of the Al/Ti interfaces during FSW and UVFSW in Fig. 14. During FSW, the $TiAl_3$ nucleated and grew at the Al/Ti interface heterogeneously, as well as coalesce into adjacent $TiAl_3$ grains, forming a non-isopachous IMC layer at the FSW interface. As ultrasonic vibrations applied during welding, an amorphous layer was formed and the Al alloy was partially oversaturated adjacent to the interface, before the formation of IMC. Subsequently, $TiAl_3$ nucleated in the amorphous layer and the Al alloy, forming $TiAl_3$ precipitates. Once the heating time lasted longer, a more isopachous $TiAl_3$ layer could be formed at the UVFSW interface, which was in accordance with previous studies [40–42].

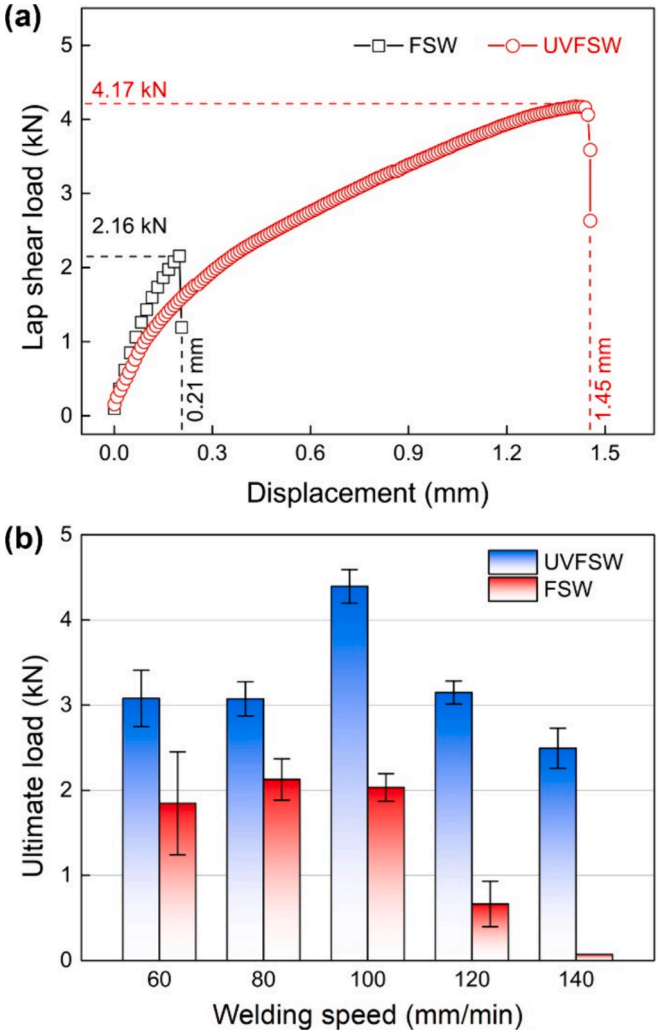

Fig. 16. Results of lap shear tests: (a) Load-displacement curves (v = 100 mm/min), (b) lap shear strength at various traversing speeds.

3.4. Mechanical properties

Microhardness was shown with the grain size in Fig. 15, and tested along the middle lines parallel to the Al/Ti interfaces of the UVFSW and FSW welds. In the HAZ, the hardness variation was closely related to the grain growth, which was caused by the welding heat. The welding temperature field was that the closer to the SZ, the higher the temperature, resulting in the coarser grains and lower hardness. Therefore,

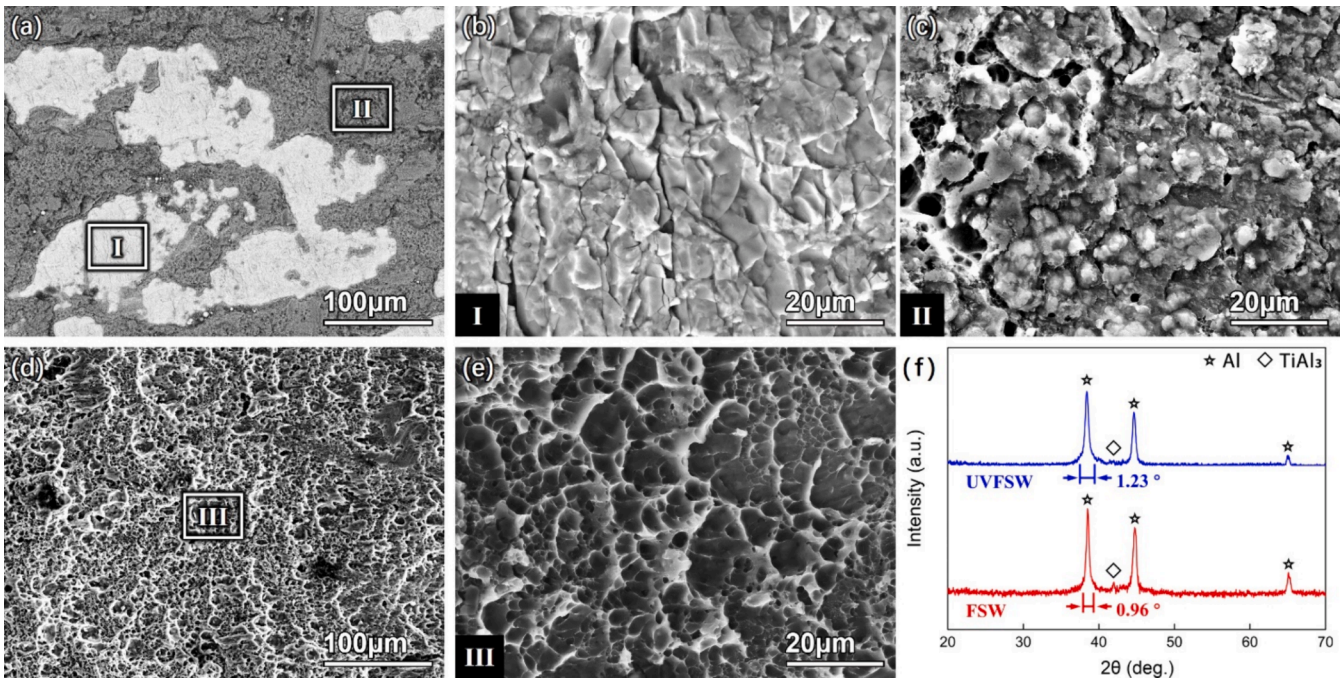

Fig. 17. Microstructure and XRD spectrums of the fracture surfaces: (a-c) fractographic images of FSW sample (v = 80 mm/min), (d-e) fractographic images of UVFSW sample (v = 100 mm/min), (f) XRD spectrums.

Table 5
Elemental compositions of the selected areas in Fig. 17.

Areas	Al	Ti	V	Mg	Si
I	96.5	0.5	0.1	2.2	0.6
II	26.7	70.2	2.1	0.5	0.6
III	85.6	11.2	0.7	1.9	0.7

along the HAZ, the hardness was declined to the ~52 HV at the TMAZ side from ~100 HV at the BM side. According to the hardness variation, the width of the HAZ of UVFSW was thinner than that of the FSW, which was attributed to the aforementioned lower welding temperature. As for the TMAZ, the microstructure consisted of large deformed grains and small recrystallized grains. Due to the strain rate gradient, the closer to the SZ, the higher the fraction of recrystallized grains. As a result, the hardness increased to ~70 HV at the SZ side of the TMAZ, due to the increase of the recrystallized grains. Due to the improvement of ultrasonic vibrations on the deformation of weld metal during welding, the hardness in the TMAZ of UVFSW was 2 HV higher than that of the FSW at the AS, and 4 HV higher at the RS. In the SZ, although the microstructure was completely recrystallized, the hardness was 71 HV±2 HV, which was ~30 HV lower than that of the BM due to the dissolution of the precipitates during welding. There was no obvious difference in SZ hardness between the UVFSW and FSW, since the grain sizes were also similar in Fig. 4.

Fig. 16 shows the lap shear tests of the Al/Ti UVFSW and FSW welds, and the shear load and displacement were recorded once per second during the tests. With the influence of ultrasonic vibrations, the maximum load of the Al/Ti welds was increased to 4.17 kN from 2.16 kN of the conventional FSW weld, with an improvement of 93.06 %. Meanwhile, the maximum displacement was improved to 1.45 mm from 0.21 mm, indicating the better plasticity of UVFSW welds. As traversing speed changed, the optimal strengths of UVFSW and FSW welds were obtained at 100 mm/min and 80 mm/min respectively, suggesting that ultrasonic vibrations could improve the welding efficiency and strength. In addition, at 140 mm/min, only one FSW sample was tested with an extremely low shear load of 0.07 kN, as the other samples were fractured during fixture gripping. The lap shear strength of UVFSW was 2.50 kN ±0.24 kN at 140 mm/min, which was much higher than that of conventional FSW. Therefore, there were opportunities to further improve the welding efficiency via UVFSW.

Fig. 17 shows the fractographic images and XRD spectrums of the FSW and UVFSW samples with maximum shear strength, and the compositions of the selected areas are listed in Table 5. Fracture surface of the FSW sample was composed of $TiAl_3$ in area I and Al alloy in area II. Area I was predominated by cleavage characteristics, suggesting the brittle fracture. This indicated that crack was propagated in the IMC layer, which was composed of $TiAl_3$ and formed at the interface as illustrated in Fig. 14. Moreover, facet was the dominant characteristic in area II, indicating that this area was fractured via interface separation. As for the UVFSW sample, fracture surface was composed of Al alloy and $TiAl_3$, while dominated by shear dimples. This indicated that the crack was propagated in the Al alloy due to the amorphous strengthened interface and the presence of Ti fragments as illustrated in Fig. 14. Compared to the cleavage fracture and interface separation, the dimple fracture would exhibit higher energy absorption as well as better ductility and plasticity, which was in accordance with the load–displacement results in Fig. 16. In addition, as compared to the conventional FSW, the Al (111) diffraction peak was expanded by 0.27° in UVFSW, due to the formation of the amorphous layer at Al/Ti interface.

4. Conclusion

Dissimilar joints of AA6061 and Ti6Al4V alloys were fabricated by UVFSW and FSW at various traversing speeds. The welding temperature and strain were analyzed. providing critical insights into the bonding mechanism of UVFSW. In addition, an interlayer, consisting of amorphous phase, was formed at the UVFSW interface, replacing and suppressing the formation of IMC. Correspondingly, the lap shear strength was improved with the improved interfacial microstructure Based on the present study, the following conclusions can be drawn.

(1) The application of ultrasonic vibrations on the substrates resulted in a reduction of the peak welding temperature, while increasing

the strain rate simultaneously. The influence of ultrasonic vibrations was more pronounced at higher traversing speeds, and it became less significant as the traversing speed was decreased.

(2) The dissimilar substrates were metallurgically bonded in UVFSW via the formation of the interfacial amorphous layer, which also suppressed the formation of IMC layer. Meanwhile, a more gradual and moderate evolution of the interfacial microstructure was formed in the UVFSW, due to elimination of microcracks and dispersion of Ti fragments at the interface.

(3) Due to the variation of the interfacial microstructure, the ultimate lap shear strength of UVFSW welds was increased to 4.17 kN, with an improvement of 93.1 %, compared to that of the conventional FSW welds in same welding condition. Meanwhile, ultrasonic vibrations also improved the fabrication efficiency with higher lap shear strength at high speeds.

(4) The failure mode shifted from interface separation of FSW welds to a shear dimple fracture of the UVFSW welds, demonstrating the better plasticity and reliability of the UVFSW Al/Ti dissimilar joints.

CRediT authorship contribution statement

Mingrun Yu: Writing – review & editing, Writing – original draft, Investigation, Formal analysis, Data curation. **Xinchen Nan:** Writing – original draft, Investigation, Data curation. **Li Zhou:** Writing – review & editing, Project administration, Funding acquisition. **Fei Xu:** Writing – original draft, Visualization, Data curation. **Hongyun Zhao:** Writing – review & editing, Supervision. **Xiaoguo Song:** Writing – review & editing, Supervision.

Declaration of competing interest

The authors declare that they have no known competing financial interests or personal relationships that could have appeared to influence the work reported in this paper.

Data availability

No data was used for the research described in the article.

Acknowledgements

This study was kindly supported by the National Natural Science Foundation of China (Grant No. 51974100) and Taishan Scholars of Shandong Province (No. tsqn202211089). The work described in this paper was partially supported by the Department of Industrial & Systems Engineering and Research Institute for Advanced Manufacturing of The Hong Kong Polytechnic University, Hong Kong SAR.

References

[1] F. Henning, L. Kärger, D. Dörr, F.J. Schirmaier, J. Seuffert, A. Bernath, Fast processing and continuous simulation of automotive structural composite components, Compos. Sci. Technol. 171 (2019) 261–279.
[2] M. Hassanalian, A. Abdelkefi, Classifications, applications, and design challenges of drones: a review, Prog. Aerosp. Sci. 91 (2017) 99–131.
[3] W. Zhang, J. Xu, Advanced lightweight materials for automobiles: a review, Mater. Des. 221 (2022) 110994.
[4] A. Heidari, N. Jafari Navimipour, M. Unal, G. Zhang, Machine learning applications in internet-of-drones: systematic review, recent deployments, and open issues, ACM Comput. Surv. 55 (2023) 1–45.
[5] A. Esmaeili, C. Sbarufatti, A.M.S. Hamouda, Characteristics of intermetallic compounds in dissimilar friction stir welding: a review, Metallography, Microstructure, and Anal. 8 (2019) 445–461.
[6] J. Pratap Kumar, A. Raj, K. Arul, V.A. Mohanavel, literature review on friction stir welding of dissimilar materials, Mater. Today:. Proc. 47 (2021) 286–291.
[7] Y. Zhang, J. Huang, Z. Ye, Z. Cheng, J. Yang, S. Chen, Influence of welding parameters on the IMCs and the mechanical properties of Ti/Al butt joints welded by MIG/TIG double-sided arc welding-brazing, J. Alloy. Compd. 747 (2018) 764–771.
[8] X. Chen, Z. Lei, Y. Chen, Y. Han, M. Jiang, Z. Tian, J. Bi, S. Lin, Microstructure and tensile properties of Ti/Al dissimilar joint by laser welding-brazing at subatmospheric pressure, J. Manuf. Process. 56 (2020) 19–27.
[9] T. Wang, X. Li, Y. Zhang, H. Li, B. Zhang, J. Feng, Regulating the interfacial morphology of electron beam welded pure Ti/2024Al dissimilar joint, J. Mater. Process. Technol. 245 (2017) 227–231.
[10] Y.M. Baqer, S. Ramesh, F. Yusof, S.M. Manladan, Challenges and advances in laser welding of dissimilar light alloys: Al/Mg, Al/Ti, and Mg/Ti alloys, Int. J. Adv. Manuf. Technol. 95 (2018) 4353–4369.
[11] R.S. Mishra, Z.Y. Ma, Friction stir welding and processing, Mater. Sci. Eng. R-Rep. 50 (2005) 1–78.
[12] R. Kumar, R. Singh, I.P.S. Ahuja, R. Penna, L. Feo, Weldability of thermoplastic materials for friction stir welding- A state of art review and future applications, Compos. B Eng. 137 (2018) 1–15.
[13] X. Meng, Y. Huang, J. Cao, J. Shen, J.F. dos Santos, Recent progress on control strategies for inherent issues in friction stir welding, Prog. Mater Sci. 115 (2021) 100706.
[14] A.S. Sundar, K.K. Mugada, A. Kumar, Enhancing microstructural, textural, and mechanical properties of Al–Ti dissimilar joints via static shoulder friction stir welding, J. Manuf. Sci. Eng. 146 (2024) 021004.
[15] Y. Yang, Z. Luo, Y. Zhang, J. Su, Dissimilar welding of aluminium to steel: A review, J. Manuf. Process. 110 (2024) 376–397.
[16] A.S. Sundar, A. Kumar, K.K. Mugada, Explication of microstructural evolution and mode of recrystallization in dissimilar Al6061–Ti6Al4V friction stir welds, Trans. Indian Inst. Met. 76 (2023) 2085–2090.
[17] A.S. Sundar, K.K. Mugada, A. Kumar, Microstructural evolution, intermetallic formation, and mechanical performance of dissimilar Al6061–Ti6Al4V static shoulder friction stir welds, Adv. Eng. Mater. 25 (2023) 2300973.
[18] A.S. Sundar, K.K. Mugada, A. Kumar, Minimizing material flow in the dissimilar joining of Al6061 and Ti6Al4V to mitigate the adverse effects of intermetallic compounds, Mater. Lett. 350 (2023) 134956.
[19] Y. Li, L. Shi, C.S. Wu, Y.N. Jiang, Achieving high property medium-thick Ti/Al dissimilar joints by double side friction stir welding, Sci. Technol. Weld. Join. 27 (2022) 655–663.
[20] H. Zhao, M. Yu, Z. Jiang, L. Zhou, X. Song, Interfacial microstructure and mechanical properties of Al/Ti dissimilar joints fabricated via friction stir welding, J. Alloy. Compd. 789 (2019) 139–149.
[21] M. Geyer, M.-N. Avettand-Fènoël, V. Vidal, F. Rezaï-Aria, C. Boher, Multi-scale effects of the tool shape and length on the interfacial microstructure and the mechanical behaviour of Al2024/Ti-6Al-4V lap friction stir welds, J. Manuf. Process. 113 (2024) 360–372.
[22] L. Zhou, M. Yu, H. Zhao, Z. Jiang, F. Guo, X. Song, Dissimilar friction stir welding of AA6061 and Ti6Al4V alloys: A study on microstructure and mechanical properties, J. Manuf. Process. 48 (2019) 119–126.
[23] Z.W. Chen, S. Yazdanian, Microstructures in interface region and mechanical behaviours of friction stir lap Al6060 to Ti–6Al–4V welds, Mater. Sci. Eng. A 634 (2015) 37–45.
[24] Y. Huang, Z. Lv, L. Wan, J. Shen, J.F. dos Santos, A new method of hybrid friction stir welding assisted by friction surfacing for joining dissimilar Ti/Al alloy, Mater. Lett. 207 (2017) 172–175.
[25] A. Kar, S.K. Choudhury, S. Suwas, S.V. Kailas, Effect of niobium interlayer in dissimilar friction stir welding of aluminum to titanium, Mater Charact 145 (2018) 402–412.
[26] A. Kar, S.V. Kailas, S. Suwas, Effect of mechanical mixing in dissimilar friction stir welding of aluminum to titanium with zinc interlayer, Trans. Indian Inst. Met. 72 (2019) 1533–1536.
[27] A. Simar, M.-N. Avettand-Fènoël, State of the art about dissimilar metal friction stir welding, Sci. Technol. Weld. Join. 22 (2017) 389–403.
[28] Z. Mao, S. Wu, X. Liu, Formation and microstructure of ultrasonic-assisted friction stir lap welding dissimilar Al-Ti alloys, Trans. China Welding Instit. 42 (2019) 145–148.
[29] Z. Ma, X. Sun, S. Ji, Y. Wang, Y. Yue, Influences of ultrasonic on friction stir welding of Al/Ti dissimilar alloys under different welding conditions, Int. J. Adv. Manuf. Technol. 112 (2021) 2573–2582.
[30] Z. Dong, Z. Zhang, W. Hu, P. Gong, Z. Lv, Microstructure and mechanical properties of friction stir lap welded dissimilar Al/Ti alloys by ultrasonic assistance, Arch. Metall. Mater. 67 (2021) 91–96.
[31] S. Kumar, C.S. Wu, G.K. Padhy, W. Ding, Application of ultrasonic vibrations in welding and metal processing: A status review, J. Manuf. Process. 26 (2017) 295–322.
[32] L. Shi, C.S. Wu, G.K. Padhy, S. Gao, Numerical simulation of ultrasonic field and its acoustoplastic influence on friction stir welding, Mater. Des. 104 (2016) 102–115.
[33] X.C. Liu, C.S. Wu, Elimination of tunnel defect in ultrasonic vibration enhanced friction stir welding, Mater. Des. 90 (2016) 350–358.
[34] L. Shi, C.S. Wu, S. Gao, G.K. Padhy, Modified constitutive equation for use in modeling the ultrasonic vibration enhanced friction stir welding process, Scr. Mater. 119 (2016) 21–26.
[35] X.C. Liu, C.S. Wu, G.K. Padhy, Characterization of plastic deformation and material flow in ultrasonic vibration enhanced friction stir welding, Scr. Mater. 102 (2015) 95–98.
[36] L. Shi, C.S. Wu, X.C. Liu, Modeling the effects of ultrasonic vibration on friction stir welding, J. Mater. Process. Technol. 222 (2015) 91–102.
[37] G.K. Padhy, C.S. Wu, S. Gao, L. Shi, Local microstructure evolution in Al 6061–T6 friction stir weld nugget enhanced by ultrasonic vibration, Mater. Des. 92 (2016) 710–723.

[38] J. Tarraf, S. Mustapha, M.A. Fakih, M. Harb, H. Wang, G. Ayoub, R. Hamade, Application of ultrasonic waves towards the inspection of similar and dissimilar friction stir welded joints, J. Mater. Process. Technol. 255 (2018) 570–583.
[39] M. Yu, H. Zhao, F. Xu, T. Chen, L. Zhou, X. Song, N. Ma, Effects of ultrasonic on friction stir Al–Ti welds: a comparative study, Sci. Technol. Weld. Join. 26 (2021) 551–558.
[40] Z. Ma, Y. Jin, S. Ji, X. Meng, L. Ma, Q. Li, A general strategy for the reliable joining of Al/Ti dissimilar alloys via ultrasonic assisted friction stir welding, J. Mater. Sci. Technol. 35 (2019) 94–99.
[41] S. Kumar, C. Wu, Suppression of intermetallic reaction layer by ultrasonic assistance during friction stir welding of Al and Mg based alloys, J. Alloy. Compd. 827 (2020) 154343.
[42] M. Yu, H. Zhao, F. Xu, T. Chen, L. Zhou, X. Song, N. Ma, Influence of ultrasonic vibrations on the microstructure and mechanical properties of Al/Ti friction stir lap welds, J. Mater. Process. Technol. 282 (2020) 116676.
[43] Y.H. Chen, Q. Ni, L.M. Ke, Interface characteristic of friction stir welding lap joints of Ti/Al dissimilar alloys, Trans. Nonferrous Met. Soc. Chin. 22 (2012) 299–304.
[44] Y.C. Chen, K. Nakata, Microstructural characterization and mechanical properties in friction stir welding of aluminum and titanium dissimilar alloys, Mater. Des. 30 (2009) 469–474.
[45] M. Liu, C. Zhang, Z. Meng, G. Zhao, L. Chen, TiAl3 nucleation mechanism and atomic-scale interface features in the Al/Ti composite structures, Compos. B Eng. 226 (2021) 109331.
[46] A. Gerlich, M. Yamamoto, T.H. North, Strain rates and grain growth in Al 5754 and Al 6061 friction stir spot welds, Metall. Mater. Trans. A 38 (2007) 1291–1302.
[47] M. Yu, H. Zhao, F. Xu, T. Chen, L. Zhou, X. Song, L.C. Chan, Effect of rotational speed on microstructure and mechanical properties of Al-Ti friction stir welds with ultrasonic vibrations, J. Mater. Process. Technol. 320 (2023).
[48] A. Kar, S. Malopheyev, S. Mironov, R. Kaibyshev, S. Suwas, S.V. Kailas, A new method to elucidate fracture mechanism and microstructure evolution in titanium during dissimilar friction stir welding of aluminum and titanium, Mater Charact 171 (2021) 110791.
[49] L. Kang, C. Yang, A review on high-strength titanium alloys: microstructure, strengthening, and properties, Adv. Eng. Mater. 21 (2019).
[50] J.C. Qiao, Q. Wang, J.M. Pelletier, H. Kato, R. Casalini, D. Crespo, E. Pineda, Y. Yao, Y. Yang, Structural heterogeneities and mechanical behavior of amorphous alloys, Prog. Mater Sci. 104 (2019) 250–329.
[51] M. Yu, H. Zhao, Z. Jiang, Z. Zhang, F. Xu, L. Zhou, X. Song, Influence of welding parameters on interface evolution and mechanical properties of FSW Al/Ti lap joints, J. Mater. Sci. Technol. 35 (2019) 1543–1554.
[52] M. Tavoosi, F. Karimzadeh, M.H. Enayati, S.H. Joo, H.S. Kim, Amorphous phase formation in Al80Fe10M10 (M = Ni, Ti, and V) ternary systems by mechanical alloying, J. Mater. Sci. 46 (2011) 7633–7638.
[53] J.H. Li, Y. Dai, Y.Y. Cui, B.X. Liu, Atomistic theory for predicting the binary metallic glass formation, Mater. Sci. Eng. R. Rep. 72 (2011) 1–28.
[54] S. Malinov, W. Sha, Z. Guo, Application of artificial neural network for prediction of time–temperature–transformation diagrams in titanium alloys, Mater. Sci. Eng. A283 (2000) 1–10.
[55] B. Milkereit, L. Giersberg, O. Kessler, C. Schick, Isothermal time-temperature-precipitation diagram for an aluminum alloy 6005A by in situ DSC experiments, Materials (basel). 7 (2014) 2631–2649.
[56] S.A. Jones, M.J. Kaufman, <Phase equilibria and transformations in intermediate titanium-aluminum alloys, Acta Metall. Mater. 41 (1993) 387–398.
[57] I. Ohnuma, Y. Fujita, H. Mitsui, K. Ishikawa, R. Kainuma, K. Ishida, Phase equilibria in the Ti–Al binary system, Acta Mater. 48 (2000) 3113–3123.
[58] C. Lin, W. Wu, Y. Han, J. Liu, M. Zhang, Q. Wang, X. Li, Orderly nucleation and competitive growth behaviors of Ti-Al intermetallic compounds in Ti/TiAl3 diffusion couple under high temperature, J. Alloy. Compd. 939 (2023) 168815.